Available online at www.sciencedirect.com
ScienceDirect
Journal of Power Sources 164 (2007) 614–623
JOURNAL OF POWER SOURCES
www.elsevier.com/locate/jpowsour

Integrated modeling and control of a PEM fuel cell power system with a PWM DC/DC converter

Song-Yul Choe [a,*], Jung-Gi Lee [b,**], Jong-Woo Ahn [a,***], Soo-Hyun Baek [c,****]

[a] *Mechanical Engineering Department, Auburn University, Auburn, AL 36848, USA*
[b] *Electrical Engineering Department, Pohang University of Science and Technology, Pohang, Republic of Korea*
[c] *Electrical Engineering Department, Dong-guk University, Seoul, Republic of Korea*

Received 26 September 2006; received in revised form 30 October 2006; accepted 31 October 2006
Available online 4 December 2006

Abstract

A fuel cell powered system is regarded as a high current and low voltage source. To boost the output voltage of a fuel cell, a DC/DC converter is employed. Since these two systems show different dynamics, they need to be coordinated to meet the demand of a load. This paper proposes models for the two systems with associated controls, which take into account a PEM fuel cell stack with air supply and thermal systems, and a PWM DC/DC converter. The integrated simulation facilitates optimization of the power control strategy, and analyses of interrelated effects between the electric load and the temperature of cell components. In addition, the results show that the proposed power control can coordinate the two sources with improved dynamics and efficiency at a given dynamic load.

Keywords: PEMFC; DC/DC PWM converter; Air, coolant and power flow control

1. Introduction

A PEM fuel cell powered system is composed of a PEM fuel cell system, a DC/DC converter with a capacitor, and a voltage-impressed inverter that controls a propulsion motor. A single cell is constructed by stacking different layers composed of bipolar plates, gas diffusion layers, catalyst and membrane. When hydrogen and oxygen chemically reacts in the catalyst, DC power is generated with heat and water as byproducts. Fig. 1 shows a typical fuel cell powered system with a PWM DC/DC converter, storage and an inverter driving the propulsion motor for mobile applications.

The open circuit voltage of a single cell is theoretically 1.23 V, but drops when a load is applied. The rapid output voltage drop is caused by increased over-potentials at the electrodes and membrane. Thus, the fuel cell exhibits a typical characteristic of a low voltage and a high current power source. If a fuel cell system should drive an electric motor via an inverter, the output voltage of the fuel cell should be stepped up to a level of the DC bus voltage that is at least equal to the peak value of the output voltage of the inverter. Boosting the voltage can be electronically carried out by a DC/DC PWM converter that, in principle, stores energy in an inductor when a switch is turned on, and discharges the energy in the inductor to a capacitor when the switch is turned off. Once the switching period is properly controlled, the voltage of the fuel cell can be boosted to the voltage level at the capacitor that can be kept constant at varying loads [1–3]. Therefore, a DC/DC converter is an indispensable part of the power system to ensure a power flow from the fuel cell to the electric machine for securing the performance and high efficiency.

The balance-of-plant (BOP) is the ancillary part that supplies fuels and coolant, also and removes the byproducts. The BOP can be divided into four subsystems: for hydrogen, air supply, water supply and heat removal. The fuel delivery system consists of a tank for hydrogen storage, while the oxygen is delivered by air through a compressor or a blower with humidifier to maintain the humidity in the cell. The heat generated is removed by a coolant circuit that includes a radiator, pump, condenser and a reservoir.

* Corresponding author. Tel.: +1 344 844 3328; fax: +1 334 844 3307.
** Corresponding author. Tel.: +82 54 279 5628.
*** Corresponding author. Tel.: +1 334 844 3346.
**** Corresponding author. Tel.: +82 2 2260 3347.
E-mail addresses: choe@eng.auburn.edu (S.-Y. Choe), baabu@postech.ac.kr (J.-G. Lee), ahnjong@auburn.edu (J.-W. Ahn), baekuniv@dongguk.edu (S.-H. Baek).

0378-7753/$ – see front matter © 2006 Elsevier B.V. All rights reserved.
doi:10.1016/j.jpowsour.2006.10.082

Nomenclature

A	area (m^2)
C	mass concentration ($kg\,m^{-3}$)
C	capacitor (F)
Cp	specific heat ($J\,kg^{-1}\,K^{-1}$)
F	Faraday number
Fr	fontal area (m^2)
h	heat transfer coefficient ($W\,m^{-2}\,{}^{\circ}C^{-1}$)
i	current density or current ($A\,cm^{-2}$ or A)
m	mass (kg)
M	molar mass ($kg\,mol^{-1}$)
n	number of cells
N	mole flux ($mol\,s^{-1}\,m^{-3}$)
N_{pl}	number of poles
P	power (W)
Q	heat transfer (J)
R_{elec}	electrical resistance (Ω)
s	entropy ($J\,mol^{-1}\,K^{-1}$)
s	balancing factor
t	thickness (m)
v, V	voltages (V)
W	mass flux ($kg\,s^{-1}\,m^{-2}$)

Superscripts, subscripts

an	anode
bl	blower
ca	cathode
cv	control volume
g	gas
i	index
membr	membrane layer
s	stator

Greek letters

ε	porosity
τ	tortuosity
η	efficiency
ϕ	flux linkage ($V\,s\,rad^{-1}$)

In addition, a load management is necessary to coordinate all aforementioned components to deliver the load power required. Four different control systems are therefore needed to obtain reliable operations of the fuel cell system as a power source.

This paper will describe the models for the fuel cell stack, air supply system, thermal circuit and a DC/DC PWM converter as key components in the system. The associated controls are briefly introduced. Finally, a new power control strategy is proposed.

2. Modeling of a fuel cell stack, air supply and thermal circuit

Fig. 2 shows a block diagram of a fuel cell powered system that includes a stack and four subsystem: hydrogen supply, air supply, water and thermal managements.

If it is assumed that the reactants are fully humidified and the hydrogen flow rate supplied is proportional to the air flow rate, the power of the stack can be only controlled by a flow rate of the air that is supplied by an electrically driven air blower. Heat produced by the stack is extracted by the coolant that in turn exchanges it with a radiator. Thus, the model for a fuel cell powered can be reduced to a stack with an air blower and the coolant circuit, and the DC/DC converter.

2.1. PEM fuel cell stack

Most fuel cell models, which describe physical behaviors of a PEM fuel cell, are described either by empirical equations fitted to the curve of the polarization characteristics or by computational fluid dynamics (CFD) to solve the mass and charges transport. The former can be used to describe a steady state behavior, but lacks the full dynamics, which is complemented by reflecting the double layer capacitor [4]. However, these models do not provide the gas dynamics dominant along flow paths. For instance, the porosity in the gas diffusion layer (GDL) causes a partial pressure drop that increases the catalyst over-potential according to the Butler–Volmer equation.

On the other hand, the CFD based models have been widely employed to analyze physical phenomena in a single cell, but limited to represent the dynamic characteristic in conjunction with components of the BOP that can be used for analysis of a power system.

Consequently, a new transient model is required. The model proposed in this paper is based on empirical equations and takes into account three major effects: the water balance in the membrane, the gas dynamics in the GDLs and the temperature distribution in a cell that is briefly described in the following sections.

2.1.1. Model improvement for the stack

A cell is constructed by individual model for layers, where the ohmic over-potential in the membrane, the activation over-potential in the catalyst on the cathode side, and the concentration over-potential are considered to obtain a current–voltage static relationship at a cell. The voltages drops for a cell are dependent on the reactant partial pressure, temperature and membrane water content.

$$v_{cell} = E(p, T) - v_{act}(p, T, i) - v_{ohm}(i, \lambda_{membr}, T) - v_{conc}(p, T, i) \quad (1)$$

$$v_{stack} = n \times v_{cell}$$

The dynamics of the fuel cell system are described with the changes of mass flows of the air and water in the fuel cell and air supply system. The results show a typical I–V characteristic of a single cell with a transient behavior mainly representing the mass transport in the air delivery system [5–8]. The dynamic behavior can be further improved by three effects: (1) water dynamics in the membrane, (2) partial pressure drop in the gas diffusion layer (GDL) and (3) temperature variation.

Water content in the membrane determines the proton conductivity. The dynamics of the water content is described by

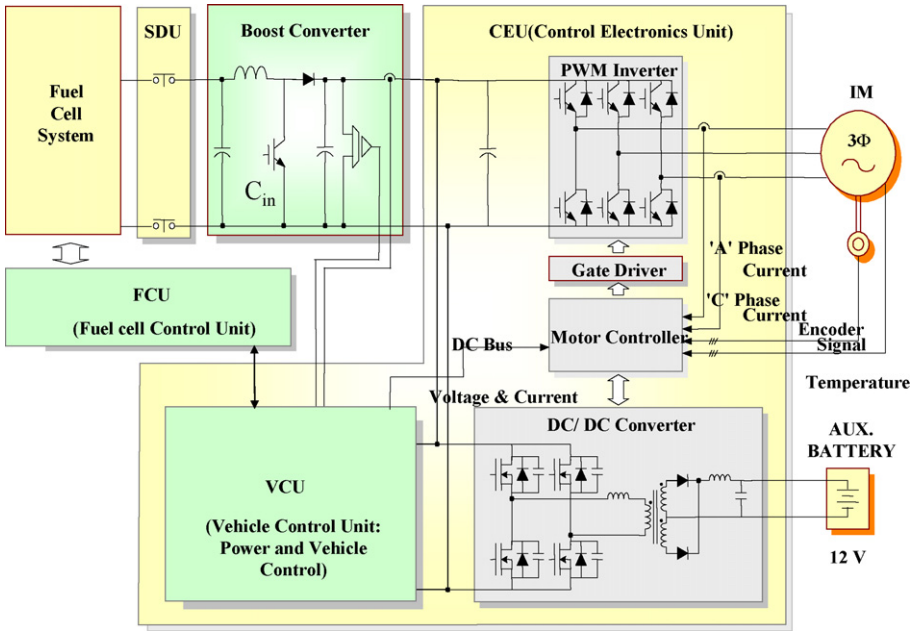

Fig. 1. Typical configuration of a PEM fuel cell powered system for automotive applications.

two effects, the electro-osmotic driving force by the different electrochemical potential at the anode and cathode, and the diffusion caused by the water concentration gradient at the two boundaries. Considering the water mass flows at the boundaries of the membrane layer, the relationship is expanded as follows [9–11]:

$$\lambda_{\text{membr}} = \frac{C_{\text{H}_2\text{O,mass}}/M_{\text{H}_2\text{O}}}{(\rho_{\text{dry,membr}}/M_{\text{membr}}) - bC_{\text{H}_2\text{O,mass}}/M_{\text{H}_2\text{O}}}$$
$$\dot{m}_{\text{water,membr}} = \frac{\text{d}(C_{\text{H}_2\text{O,mass}} A_{\text{cell}} t_{\text{membr}})}{\text{d}t} = W_{\text{ele,membr,an}} - W_{\text{ele,membr,ca}} + W_{\text{diff,membr,an}} + W_{\text{diff,membr,ca}} \quad (2)$$

On the other hand, the reactant entering the cell diffuses through the GDL before reaching the catalyst layer that significantly affects the overall dynamics of the reactants. This diffusion effect is reflected by using the mass continuity (3) and the Stefan–Maxwell Eq. (4) [4]:

$$\frac{\varepsilon_{\text{g}}}{RT}\frac{\partial p_i}{\partial t} + \frac{\partial N_i}{\partial y} = 0 \quad (3)$$

$$\frac{\varepsilon_{\text{g}}}{\tau^2}\frac{\partial p_i}{\partial y} = \sum_{k=1}^{3} \frac{RT}{p_{\text{ca}} D_{ik}} (p_i N_k - p_k N_i) \quad (4)$$

Hence, $i, k \in (1, 3)$, where p_1 is the oxygen partial pressure, and $p_2 = p_{\text{sat}}(T)$ and p_3 are the water vapor and the nitrogen partial pressure, respectively. The diffusion coefficients of $p_{\text{ca}}D_{ik}$, $D_{ik,\text{orin}}$ and $D_{ik,\text{orin}}(T)$ include the cathode pressure of p_{ca}, summing the species partial pressures. The parameter τ is a constant describing the pore curvature of GDL.

If a cell is assembled with cubical layers, where the thermophysical properties are isotropic and constant, then according to the energy conservation equation, the total energy changes in

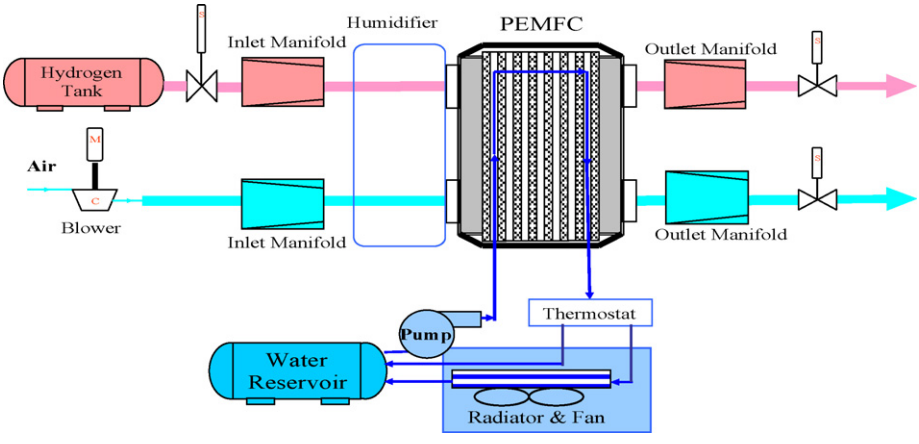

Fig. 2. A schematic diagram of a PEM fuel cell system.

Table 1
Simulation parameters

Fuel cell		
n	381	
A_{FC} (cm^2)	280	
Proton conducting model		
b_{11}	0.5139	[7]
b_{12}	0.326	[7]
b_2	350	[7]
n_d	$f(C_{water})$	[7]
D_w	$f(T, C_{water})$	[7]
Gas transport model		
D_{eff} ($m^2\ s^{-1}$)	$f(P, T)$	[5]
p_{sat}	$f(T)$	[5]
Electrochemical reaction model		
p_0 (bar)	1.0	
T_{ref} (K)	353.15	
E_{ref} (V)	1.229	[19]
$A_{catl,eff}/A_{cell}$	$f(I, T, P_{o2})$	[19]
Thermal model		
H_{gas}	$f(P, T)$	[13]
Cp_{gas}	$f(P, T)$	[13]
ρ_{gas}	$f(P, T)$	[13]
Fr_{area} (m^2)	1	
M_{res} (kg)	5	
hA ($J\ K^{-1}$)	16.66	

	Thickness (m)	Density ($W\ mK^{-1}$)	Heat conductivity ($J\ kg^{-1}\ K^{-1}$)	Specific heat ($kg\ m^{-3}$)
Geometrical data for layers [13]				
Coolant channel	0.002	1400	30	935
Plate	0.001	1400	52	935
Gas channel	0.001	1400	52	935
GDL	0.0004	2000	65	840
Catalyst layer	0.000065	387	0.2	770
Membrane layer	0.0001275	1967	0.21	1100

a controlled volume are equal to the sum of energy exchange at boundaries and internal energy resources. In fact, the energy exchanges at boundaries occur by three factors: (a) the mass flow into each volume; (b) the conduction heat transfer across the cell; (c) the convection heat transfer occurring between bipolar plates with the coolant and the reactants. Thus, the thermal-dynamic behavior can be described with the following energy conservation Eq. (5) [11]:

$$\sum_i Cp_i \rho_{i,mass} A_{cell} t_{cv} \frac{dT_{cv}}{dt} = \underbrace{\sum W_{in} A_{cell} Cp_j (T_{in} - T_{cv})}_{\text{mass flow in}} + \underbrace{\dot{Q}_{conv} A_{cell}}_{\text{convection heat transfer}} + \underbrace{\dot{Q}_{cond} A_{cell}}_{\text{convection heat transfer}} + \underbrace{\dot{Q}_{sou}}_{\text{sources}} \quad (5)$$

On the other hand, the internal energy source is composed of entropy loss and the chemical energy required for protons to overcome the barrier of the over-potentials in both catalyst layers (6). In addition, others are ohmic losses caused by a transport of electrons and protons in the cell [12]:

$$\dot{Q}_{sou} = i A_{cell} \left(-\frac{T\Delta s}{4F} + \eta + i A_{cell} R_{elec} \right) \quad (6)$$

All models were coded by blocks given in MATLAB/Simulink.

2.1.2. Parameters and simulation

The parameters and reference data for the models chosen are as follows (Table 1), which are partially empirical [4,6,12,18]. In addition, the maximum voltage and current used for this study are 0.95 V and 0.95 A cm^{-2}, respectively.

Multi-run simulations have been conducted to investigate the static and dynamic behavior of a single cell. The static behavior is analyzed by calculating the typical polarization at different temperatures shown in Fig. 3 and temperature distribution at a constant current. Only the *I–V* characteristic is taken at the varied temperatures from 333 to 353 K with a step of 10 K. As the temperature rises, the water removal is eased. Specially, the effects are considerably high at the range of the high cell current where more water is produced. This result is comparable with the CFD analysis [13].

Fig. 4 shows the temperature distribution through the cell at seven minutes. The temperature changes dynamically and

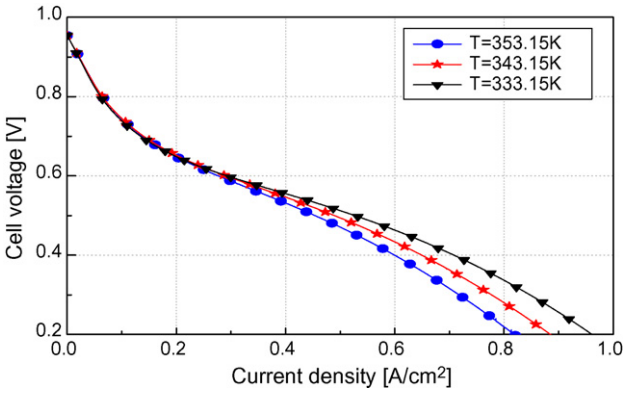

Fig. 3. *I–V* curve for different cell working temperature cell: $p = 1.0$ bar.

consequently the voltage of a cell is no loner assumed to be constant at a given load. Particularly, the temperature in the catalyst on the cathode side shows the highest peak among others because of the losses associated with the higher over-potential

$$W_{\mathrm{bl}} = \begin{cases} \omega_{\mathrm{bl}}(-20.581(p^*)^2 - 1.4415 \times 10^{-3} p^* + 4.1333 \times 10^{-5}), & p^* \le 9 \times 10^{-4}\ \mathrm{Pa\,s^2\,rad^{-2}} \\ \omega_{\mathrm{bl}}(-1.7973 p^* + 1.6409 \times 10^{-3}) & \text{otherwise,} \end{cases} \tag{9}$$

than the anodic one. The maximum temperature difference between the catalyst at the cathode side and the coolant channel is 7 K.

2.2. Air supply system

The air supply system consists of a blower, a humidifier, plumbing for the inlet and the outlet. The outlet of a blower driven by an electric motor is connected to a humidifier and an inlet of flow channels through pipes. In this study, the humidifier is simplified as an ideal one without any associated dynamics and energy losses.

The blower is constructed with an impeller driven by an electric motor. The dynamic response of the blower is described by the inertia of the motor and the impeller, and the torque produced by the motor. Hence, the torque produced by the motor, $\tau_{\mathrm{bl,m}}$, is a function of the stator resistance, $R_{\mathrm{s,bl,m}}$ (Ohm), magnetic flux constant, $\Phi_{\mathrm{bl,m}}$ (V s rad^{-1}), and the number of the poles, $N_{\mathrm{bl,m,pl}}$ with the stator voltage, $V_{\mathrm{bl,m}}$ (V), (8) [14]. Therefore, the flow rate (W_{bl}) can be controlled by the voltage

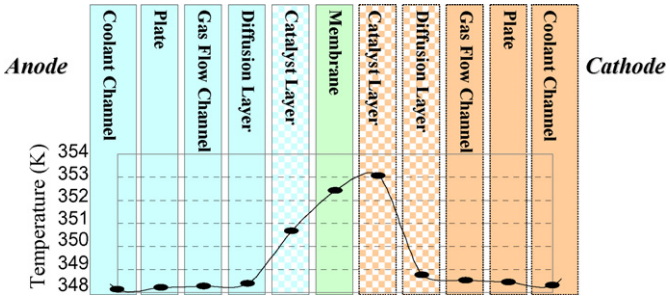

Fig. 4. Temperature distribution in the cell at 7 min after a startup (left to right: anode coolant channel to cathode coolant channel).

of the motor, $V_{\mathrm{bl,m}}$ (V).

$$\frac{\mathrm{d}\omega_{\mathrm{bl}}}{\mathrm{d}t} = \frac{1}{J_{\mathrm{bl}}}\left(\tau_{\mathrm{bl,m}} - \frac{W_{\mathrm{bl}}\Delta p_{\mathrm{bl}}\eta_{\mathrm{bl}}}{\eta_{\mathrm{bl}}\rho_{\mathrm{amb}}\omega_{\mathrm{bl}}}\right) \tag{7}$$

$$\tau_{\mathrm{bl,m}} = \eta_{\mathrm{bl,m}}\frac{3}{2}\left(\frac{N_{\mathrm{bl,m,pl}}}{2}\right)\left(\frac{\Phi_{\mathrm{bl,m}}}{R_{\mathrm{s,bl,m}}}\right) \times \left[V_{\mathrm{bl,m}} - \left(\frac{N_{\mathrm{bl,m,pl}}}{2}\right)\Phi_{\mathrm{bl,m}}\omega_{\mathrm{bl}}\right] \tag{8}$$

where ω_{bl} is the angular velocity (rad s^{-1}), J_{bl} the rotational inertia (kg m^2), $\eta_{\mathrm{bl,m}}$ the motor efficiency, p_{bl} the pressure (Pa) and ρ_{amb} is the density (kg m^{-3}).

The parameters for the blower are derived by characteristic data and specifications given by Phoenix Analysis & Design Technologies (PADT) [15], which includes both the flow parameter and overall efficiency versus the head parameter. The equations describing the behavior of the impeller are given as follows [14]:

$$\eta_{\mathrm{bl}} = -2.8831 \times 10^{13}\left(\frac{W_{\mathrm{bl}}}{\omega_{\mathrm{bl}}}\right)^3 + 9.5115 \times 10^{8}\left(\frac{W_{\mathrm{bl}}}{\omega_{\mathrm{bl}}}\right)^2 + 1.3087 \times 10^{4}\left(\frac{W_{\mathrm{bl}}}{\omega_{\mathrm{bl}}}\right) + 0.17945 \tag{10}$$

where p^* is $((p_{\mathrm{ca}} - p_{\mathrm{amb}})/\omega_{\mathrm{bl}}^2)^2$.

The inlet and outlet manifold pressures are governed by the mass conservation equation:

$$\dot{p}_{\mathrm{im}} = \frac{\gamma R_{\mathrm{a}}}{V_{\mathrm{im}}}(W_{\mathrm{bl}}T_{\mathrm{bl}} - W_{\mathrm{im,out}}T_{\mathrm{im}}) \tag{11}$$

$$\dot{p}_{\mathrm{om}} = \frac{R_{\mathrm{a}}T_{\mathrm{om}}}{V_{\mathrm{om}}}(W_{\mathrm{ca,out}} - W_{\mathrm{om,out}}) \tag{12}$$

2.3. Thermal system

The thermal system serves to reject the excess heat produced by losses in the stack. The major components of the circuit are a radiator for heat exchange with the ambient, and a fan to increase effectiveness of the heat by convection and radiation, and a water reservoir to store and to insulate the coolants thermally. Finally, a pump serves to supply the coolant to the heat source. The models for these components are based on the principle of heat transfer. Kroger [16] proposed a heat transfer coefficient, h_{rad}, (kW m^{-2} °C^{-1}) and pressure drop, p_{r} (kPa) of a radiator as a function of the air mass flow rate W_{air} (kg s^{-1}):

$$h_{\mathrm{rad}} = -1.4495W_{\mathrm{air}}^2 + 5.9045W_{\mathrm{air}} - 0.1157 \tag{13}$$

$$p_{\mathrm{r}} = (326.12W_{\mathrm{air}} - 75.396) + 101.325 \tag{14}$$

If the heat of the coolant is fully transferred to the radiator without any losses, the heat capacity of the coolant is identical with that of the radiator. Therefore, the outlet temperature of the

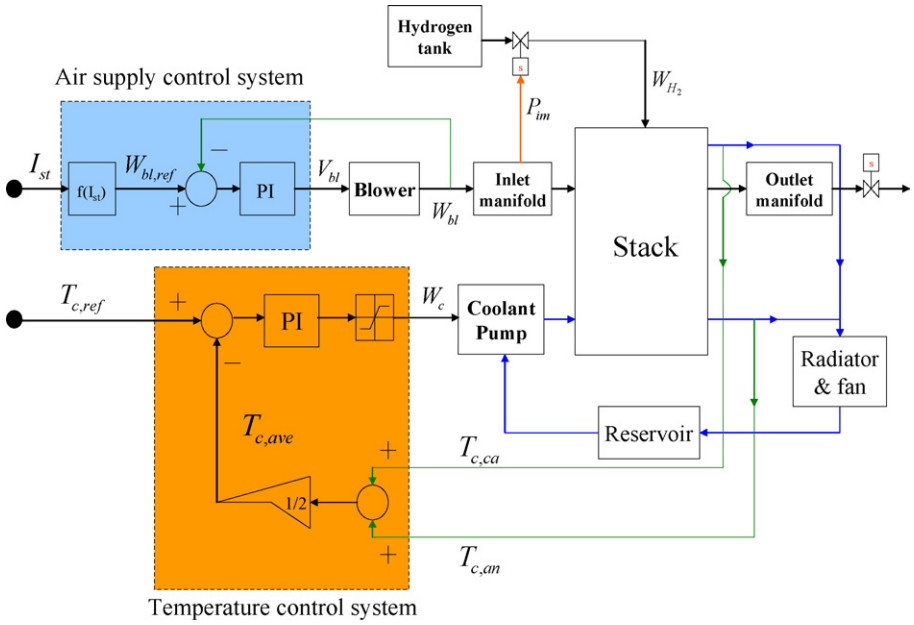

Fig. 5. Air and coolant controls.

coolant can be expressed as a function of the radiator geometry, the temperature drop between the inlet and outlet, and the heat convection caused by the temperature difference between the ambient and the outgoing air temperature [16]:

$$T_{\mathrm{rad,c,out}} = T_{\mathrm{rad,c,in}} - 0.5\left(\frac{\mathrm{Fr_{area}}(T_{\mathrm{rad,c,in}})h_{\mathrm{rad}}}{W_{\mathrm{c}}\mathrm{Cp_c}}\right) \tag{15}$$

where $\mathrm{Fr_{area}}$ denotes the frontal area ($\mathrm{m^2}$) of the radiator, and $T_{\mathrm{rad,c,in}}$ denotes the stack outlet temperature of the air. And the electric power for the fan can be calculated according to a thermal dynamic relationship between pressure drop and air flow rate [12]:

$$P_{\mathrm{fan}} = \frac{1}{\eta_{\mathrm{elec}}\eta_{\mathrm{fan}}}\left(W_{\mathrm{air}}\mathrm{Cp_{air}}T_{\mathrm{amb}}p_{\mathrm{r}}{}^{((k-1)/k)-1}\right) \tag{16}$$

where P_{fan} denotes the electric power (W) and η does the efficiency of the fan and the fan motor.

The reservoir should be insulated thermally after the heat exchange occurs at the radiator by the convection. The variation of the heat in the reservoir is the sum of the heat that the coolant carries and the heat exchanging with the ambient. Accordingly, the outlet temperature at the end of the given time interval can be expressed by the following equation [12]:

$$T_{\mathrm{res,out}} = T_{\mathrm{res,p}} - \frac{\Delta t}{M_{\mathrm{res}}\mathrm{Cp_{res}}}(W_{\mathrm{c}}\mathrm{Cp_c}(T_{\mathrm{res,p}} - T_{\mathrm{res,in}}) + hA(T_{\mathrm{res,in}} - T_{\mathrm{amb}})) \tag{17}$$

where T_{res} is the outlet temperature of a reservoir at the end of a time step (K), $T_{\mathrm{res,p}}$ the temperature of the reservoir at the previous of time step (K), Δt the time interval (s), M_{res} an equivalent mass of the coolant in the control volume (kg), hA the heat transfer of plumbing to ambient and $T_{\mathrm{res,in}}$ is the temperature of coolant into reservoir (K), respectively.

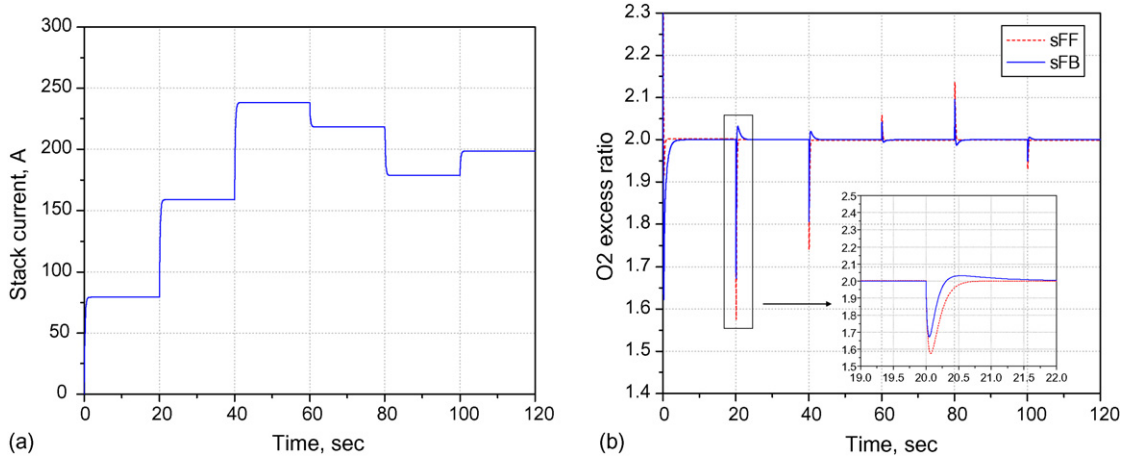

Fig. 6. Comparison between sFF and sFB (a) load current; (b) oxygen excess ratio.

The coolant pump should deliver the coolants from the reservoir and at the same time from the stack to radiator. If it is assumed that all heat energy generated in the stack is completely transferred to the coolant, then the mass flow rate of the coolant is expressed by its relationship with the heat source.

$$W_c = \frac{\dot{Q}_{sou}}{Cp_c\,\Delta T} \tag{18}$$

2.4. Controls for the air and coolant flow rate

Fig. 5 depicts a system configuration that includes two conventional PI controllers to control the flow rate of the air and the coolant.

Pukrushpan et al. [17] proposed different control strategies for the air supply system to maintain the optimal oxygen excess ratio to prevent an oxygen starvation during abrupt changes of the load current. Hence, the oxygen excess ratio is defined as the oxygen supplied by the one consumed. Two control strategies, a static feed-back (sFB) and a static feed-forward (sFF) have been implemented and compared in Fig. 6. It turns out that the sFB demonstrates better performance with respect to the marginal limit of an oxygen starvation and a quick recovery behavior. Hence, the working temperature of the cell is assumed to be constant.

When the load current varies abruptly, the temperature in the stack rises, particularly in the catalyst shown in Fig. 7. In addition, Fig. 7 shows the temperature in the catalyst and coolant channel, where the temperature of the coolant is well controlled. According to the analyses conducted, the temperature in the catalysts on the cathode side is 3–8 °C higher than the average temperature of a stack dependent upon load current. The temperature in the catalysts is not measurable. Therefore, the actual temperature of the stack necessary for the controls is taken from the one at the outlet of the anode and the cathode side that has been averaged. The reference temperature of the stack is set to 77 °C.

It is observed that the oxygen excess ratio at the cell with varying temperature has increased, which results from different working temperature between the empirical mode and the model proposed. The temperature in the gas channel is low because of the cooling effect. Thus, the oxygen excess ratio shows a value of 2.07 with an offset.

In addition, the oxygen excess ratio varies inversely as the current increases or decreases. At an increased current, more heat in the catalyst is generated and consequently the temperature in each of layers rises. In fact, the temperature of the coolant is the same as the reference value. Therefore, the temperature in the flow channel tends to rise as the load current increases and the partial pressure in the gas channel rises. Consequently, the mass of the air becomes less and the associated oxygen excess ratio gets lower. Likewise, the oxygen excess ration gets higher as the current is decreases.

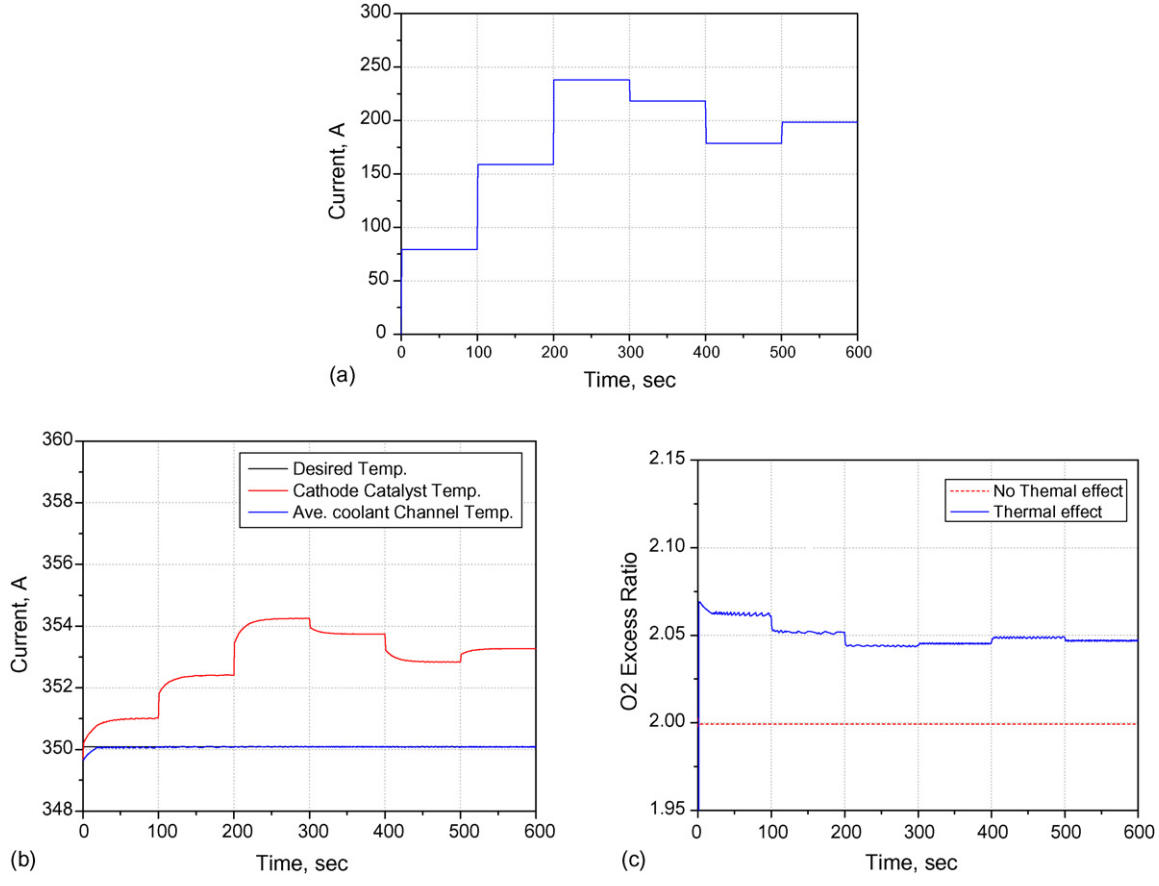

Fig. 7. (a) Step current; (b) catalyst and coolant temperature; (c) oxygen access ratio.

3. DC/DC converter

A typical configuration of a fuel cell powered system with a DC/DC converter is shown in Fig. 1. The PWM DC/DC converter can be described by using two state Eqs. (19) and (20), if the operation is limited to a conduction mode and no losses occur at the power conversion [19–21].

$$\frac{dv_{DC}}{dt} = \frac{1}{C}i_{cap} = \frac{1}{C}(1-D)i_{FC} - \frac{v_{DC}}{CR_{load}} \tag{19}$$

$$\frac{di_{FC}}{dt} = \frac{1}{L}(v_{FC} - (1-D)v_{DC}) = \frac{1}{L}(v_{FC} - v_1) \tag{20}$$

where v_1 denotes the average voltage at the lower switch during pulse width modulation (PWM) period, D the switching on-duty period, v_{FC} the output voltage of the fuel cell system and v_{DC} the output voltage of the converter, respectively.

With no losses in the converter, the input power of the converter, $P_{FC} = i_{FC}v_{FC}$, is identical to the output power of the converter, $P_{con} = i_{con}v_{DC}$. Then, the current at the output and the capacitor result is as follows:

$$i_{con} = \frac{P_{FC}}{v_{DC}} = \frac{v_{FC}i_{FC}}{v_{DC}} \tag{21}$$

$$i_{cap} = i_{con} - i_{load} \tag{22}$$

$$i_{con} = \frac{v_{FC}i_{FC}}{v_{DC}} - i_{load} \tag{23}$$

The equations above present a second order linear system with two state variables, the DC output voltage v_{DC} and the fuel cell current i_{FC}. A block diagram for the controls of the PWM DC/DC converter is shown in Fig. 8. For the voltage control loop, a feed-forward controller is employed to increase control dynamics on the voltage variation which directly feeds the reference voltage to the reference for the modulation.

For the current loop, a proportional controller and integrator (PI) are used. The control variable for the loop is the current in the capacitor, which ultimately facilitates a complete control of the DC voltage. It is necessary to consider the dynamic of the load current, where the capacitor current is the difference between the output current and the load current drawn. Therefore, the load current is added, as shown in Fig. 5. The equations for the controls are given as follows:

$$v_1^* = -\left(k_{p1} + \frac{k_{i1}}{s}\right)(i_{cap}^* - i_{cap}) + v_{FC} \tag{24}$$

$$i_{cap}^* = \left(k_{p2} + \frac{k_{i2}}{s}\right)(v_{DC}^* - v_{DC}) \tag{25}$$

The gains for the current loop have been particularly designed to increase the bandwidth of the closed-loop as high as possible to dynamically respond to any load changes. Conversely, the gains for the voltage loop are designed by considering the slow dynamics of the fuel cell system as a power source:

$$G(s)_{\text{closed loop}} = \left.\frac{v_{DC}}{v_{DC}^*}\right|_{i_{load}=0} = \frac{G_1 + G_2}{\Delta} \tag{26}$$

where

$$\Delta = LCs^4 + K_{p2}C(1-D)s^3 + (K_{p1}K_{p2} + K_{i2}C)(1-D)s^2 + (K_{p1}K_{i2} + K_{p2}K_{i1})(1-D)s + K_{i1}K_{i2}(1-D),$$
$$G_1 = K_{p2}K_{p2}(1-D)s^2 + (1-D)(K_{p1}K_{i2} + K_{p2}K_{i1})s + K_{i1}K_{i2}(1-D),$$
$$G_2 = D(1-D)K_{p2}s^2 + D(1-D)K_{i2}s.$$

4. Power control of the PEM fuel cell system with the DC/DC converter

The objective of the power flow control is to accurately supply the power required from the load, thereby maximizing overall system efficiency and at the same time maintain the voltage level of the DC at the capacitor, which should not deteriorate the performance of the motor drive system. On the other hand, there are two energy sources available that can be combined to operate efficiently [22,23]. The total power that the system can supply is a sum of the energy stored in the DC capacitor and the power generated by the stack, which can be expressed as follows:

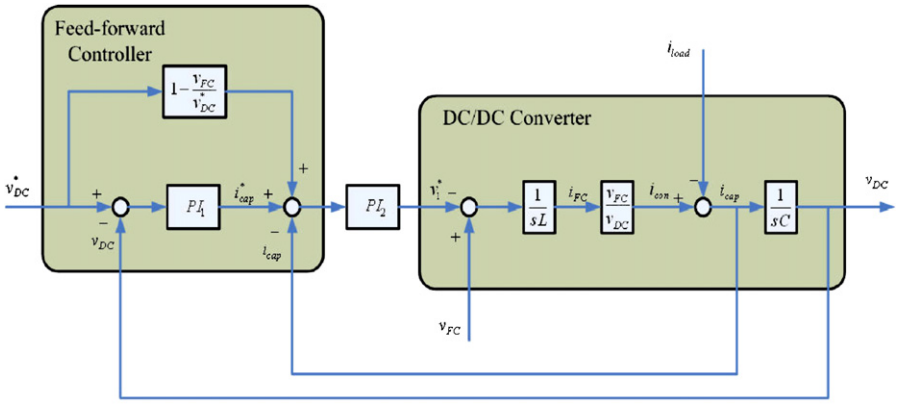

Fig. 8. Control block diagram for the PWM DC/DC converter.

Table 2
Simulation parameters for the DC/DC converter

Switching frequency (kHz)	20	IGBT forward voltage (V)	1
V_{DC} (V)	500	IGBT off current tail time (s)	4×10^{-6}
C (μF)	1500	IGBT on (s)	0.017
C_{in} (μF)	350	Diode on (Ω)	0.015
L (μH)	240	Diode forward voltage (V)	0.8
R_{load} (Ω)	6.25–62.5	Calculation step size (s)	1×10^{-6}

If a ratio of both power is defined as a new variable, s, then,

$$P_{total}(t) = P_{FC}(t) + P_{DC}(t) = sP_{DC}(t) + P_{DC}(t) = (s+1)P_{DC}(t) \quad (27)$$

The variable, s, determines a factor responsible for the power split between the fuel cell and the capacitor, which can be controlled according to the efficiency and the power being supplied by the capacitor.

When the derivative of the DC voltage is negative, the capacitor needs to be recharged from the stack. Otherwise, the DC capacitor is able to supply only a certain amount of power to the load. Then the reference power for the fuel cell stack is adjusted by a new value of the variable, s, which is determined by an efficiency map of the stack stored. Therefore a new reference for the stack current, I^*_{FC}, is generated by a division of the DC power and the output voltage of the stack, which is expressed as follows:

$$P^*_{DC} = (sx(t) + s(x(t)-1))P_{DC}$$
$$x(t) = \begin{cases} 0 : \frac{v_{DC}}{dt} < 0 \\ 1 : \frac{v_{DC}}{dt} > 0 \end{cases} \quad (28)$$

$$I^*_{FC} = \frac{(1+s(t))P^*_{DC}}{V_{FC}} \quad (29)$$

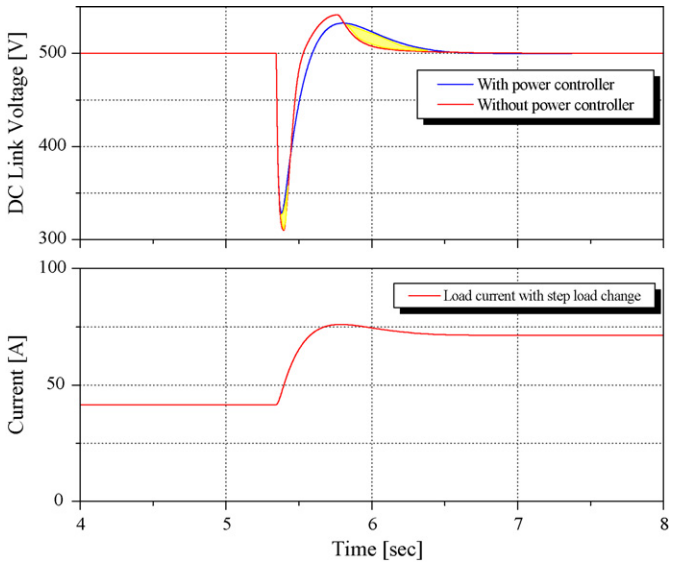

Fig. 9. DC voltage with the power control.

5. Integration and simulation

Integration of this power system is conveyed on a real-time system in order to reduce the computational time. The fuel cell system is connected through a voltage source control block, where the current at the inductor is set to the reference current for the stack that controls the air flow rate. Subsequently, the output voltage of the stack is adjusted according to the dynamics described. The output voltage and power of the stack at the operating power approximately 250 V. The models developed are implemented with the software package of MATLAB/Simulink/Simpower. The parameters used for the simulation are summarized in Table 2.

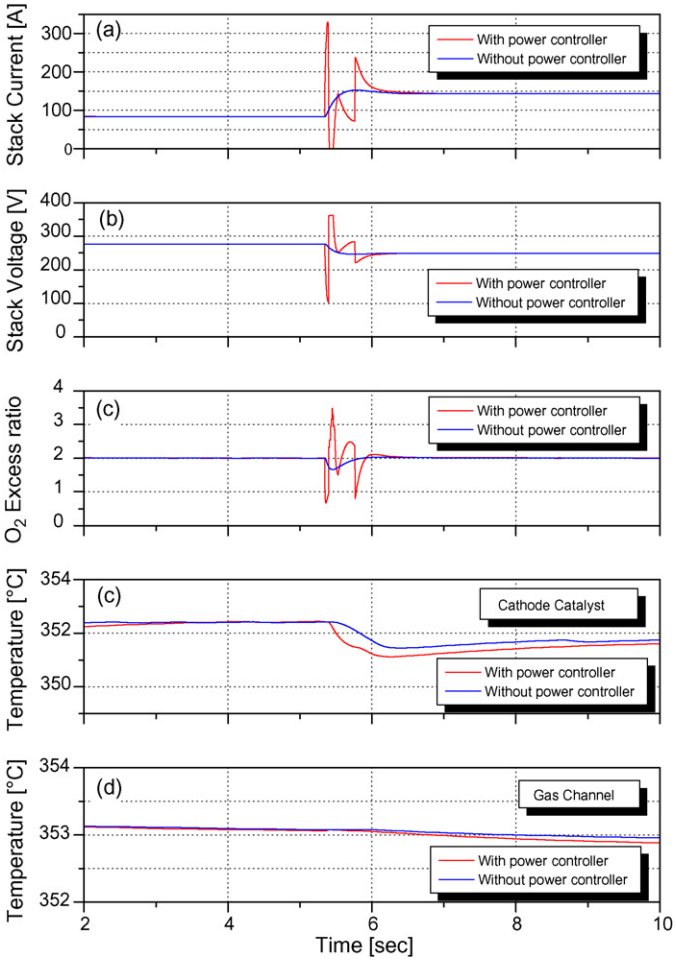

Fig. 10. Dynamic response of the fuel cell power system at a step load with the power control.

Fig. 9 demonstrates the effects of the power control when the load current dynamically changes from 40 to 70 A. The yellow areas present the contribution of the energy stored in the capacitors. When a load is applied, the voltage at the capacitor drops and the stack immediately reacts to refill the voltage gap by supplying the current. At the same time, the capacitor is being charged and the voltage at the capacitor increases. Then, the supply of the power from the stack is reduced to operate the stack more efficiently by the energy stored in the capacity. The switching mechanism repeats until the voltage reaches to the set steady state.

Fig. 10 shows the simulated results for the current, voltage, oxygen excess ratio, temperature in the cathode catalysts as well as the gas flow channel of a fuel cell stack. When a step-like current is applied, the current and voltage of the stack follow the load changes with a time constant determined by the air supply system. When the new power controller is employed, the reference values for the stack current and voltage is continuously shifted to get an efficient operating point. Accordingly, the current and voltage varies dynamically and subsequently the oxygen excess ratio as well. However, it turns out that the temperature rise in the catalysts during the transition gets slightly lower than the one without power controller, which indicates reduced losses in the cell. At the same time, the temperature in the gas flow channel gets lower even at the increased load.

6. Conclusion

The paper presented has attempted to integrate component models for a PEM fuel cell power system that includes a stack, air supply system, thermal circuit and a PWM DC/DC converter as well as the associated control strategies. The integration reveals a variety of possibilities to study design parameters of a fuel cell powered system, particularly to consider a realistic characteristic of the fuel cell system along with an air supply system and the associated controls. A summary of new findings obtained is as follows:

- the dynamic model for the stack currently used for controlling a power system can be improved by adding water balance in the membrane, diffusion effect in the GDL and temperature effects;
- the oxygen excess ratio is inversely influenced by the load profile because of the change of the partial pressure in the gas flow channel;
- the dynamics and efficiency can be improved when the energy stored in capacitor is utilized to continuously shift the operating point of the stack to a high efficient area;
- real time simulation with the fuel cell stack and the DC/DC converter enables a reduction of the computational time in two orders of magnitude that provides a new way to implement the automotive power system and analyze interacting effects between the electric load and the individual components of a cell.

Future work will include: (1) integration of a bypass valve in the thermal circuit, (2) improvement of temperature control to effectively reduce temperature rise in the catalyst, (3) compensation of the temperature effect on the oxygen excess ratio and (4) advanced power management taking into account the fuel cell dynamics and efficiency.

Acknowledgement

The research is supported by the Korean Government, Department of Commerce, Industry and Energy under a grant for Korea–US collaboration.

References

[1] N. Mohan, T.M. Undeland, W.P. Robbins, Power Electronics, Converters, Applications and Design, John Wiley & Sons, Inc., Canada, 1995.
[2] C. Gezgin, B.S. Heck, R.M. Bass, 28th Annual IEEE Power Electronics Specialists Conference, vol. 2 (1997) 901–907.
[3] H. Rudnick, J. Dixon, L. Moran, Power Energy Mag., IEEE 1 (2003) 32–40.
[4] M. Ceraolo, C. Miulli, A. Pozio, J. Power Sources 113 (2003) 131–144.
[5] T.V. Nguyen, R.E. White, J. Electrochem. Soc. 140 (1993) 2178–2186.
[6] T.E. Springer, T.A. Zawodzinski, S. Gottesfeld, J. Electrochem. Soc. 138 (8) (1991) 2334–2342.
[7] J.H. Le, T.R. Lalk, J. Power Sources 73 (1998) 229–241.
[8] L. Guzzella, NSF Workshop on the Integration of Modeling and Control for Automotive Systems, 1999.
[9] J.C. Amphlett, R.M. Baumert, R.F. Mann, B.A. Peppley, P.R. Roberge, A. Rodrigues, J. Power Sources 49 (1994) 349–356.
[10] J.T. Pukrushpan, H. Peng, A.G. Stefanopoulou, Proceedings of IMEXE'01 2002 ASEM International Mechanical Engineering Congress & Exposition, New Orleans, LA, 2002.
[11] Yuyao Shan, S.Y. Choe, J. Power Sources 158 (2006) 274–286.
[12] S. Gurski, Master of Science Thesis, Virginia Polytechnic Institute and State University, 2002.
[13] J.C. Amphlett, E.H. deOliveira, R.F. Mann, P.R. Roberge, A. Rodrigues, J.P. Salvador, J. Power Sources 65 (173) (1997).
[14] P.C. Krause, O. Wasynczuk, Electromechanical Motion Devices, 1st ed., McGraw-Hill Book Company, New York, 1989.
[15] Phoenix Design & Technologies, 2005. The PDAT Turbomix. http://www.padtinc.com/sales/fuelcell/turbomix/, August 2006.
[16] D.G. Kroger, #840380 SAE Trans. 93 (1984) 2984–2990.
[17] J.T. Pukrushpan, A.G. Stefanopoulou, H. Peng, Proceedings of American Control Conference, Anchorage, Alaska, 2002.
[18] J.C. Amphlett, R.M. Baumert, R.F. Mann, B.A. Peppley, P.R. Roberge, J. Electrochem. Soc. 142 (1) (1995) 9–15.
[19] W.J. Choi, P.N. Enjeti, J.W. Howze, Applied Power Electronics Conference and Exposition, APEC'04, Nineteenth Annual IEEE, vol. 1, 2004, pp. 355–361.
[20] A.J. Forsyth, S.V. Mollov, Power Eng. J. 12 (October (5)) (1998) 229–236.
[21] D. Logue, P.T. Krein, The Seventh Workshop on Computers in Power Electronics, July, 2000, pp. 34–39.
[22] J. Schiffer, O. Bohlen, R.W. De Doncker, D.U. Sauer, K.Y. Ahn, Vehicle Power and Propulsion 2005 IEEE Conference, September 7–9, 2005.
[23] P. Thounthong, S. Raël, B. Davat, J. Power Sources (2005).